

The source of the 2017 cosmic ray half-year modulation event

O.P.M. ASLAM ¹, D. MACTAGGART ¹, R. BATTISTON ², M.S. POTGIETER ³, AND M.D. NGOBENI ⁴

¹*School of Mathematics and Statistics, University of Glasgow, Glasgow G12 8QQ, United Kingdom*

²*Department of Physics, University of Trento, Povo, Italy*

³*Institute for Experimental and Applied Physics (IEAP), Christian-Albrechts-University of Kiel, 24118 Kiel, Germany*

⁴*Centre for Space Research, North-West University, 2520 Potchefstroom, South Africa*

ABSTRACT

In 2017, as the solar cycle approached solar minimum, an unusually long and large depression was observed in galactic cosmic ray (GCR) protons, detected with the Alpha Magnetic Spectrometer (AMS-02), lasting for the second half of that year. The depression, as seen in the Bartel rotation-averaged proton flux, has the form of a Forbush decrease (FD). Despite this resemblance, however, the cause of the observed depression does not have such a simple explanation as FDs, due to coronal mass ejections (CMEs), typically last for a few days at 1 AU rather than half a year. In this work, we seek the cause of the observed depression and investigate two main possibilities. First, we consider a minicycle - a temporary change in the solar dynamo that changes the behaviour of the global solar magnetic field and, by this, the modulation of GCRs. Secondly, we investigate the behaviour of solar activity, both CMEs and corotating/stream interactions regions (C/SIRs), during this period. Our findings show that, although there is some evidence for minicycle behaviour prior to the depression, the depression is ultimately due to a combination of recurrent CMEs, SIRs and CIRs. A particular characteristic of the depression is that the largest impacts that help to create and maintain it are due to four CMEs from the same, highly active, magnetic source that persists for several solar rotations. This active magnetic source is unusual given the closeness of the solar cycle to solar minimum, which also helps to make the depression more evident.

Keywords: Active regions — Solar coronal mass ejections — Solar coronal holes — Solar wind — Space weather — Cosmic rays

1. INTRODUCTION

Galactic cosmic rays (GCRs) are high energy particles of galactic origin that become modulated inside the heliosphere by the solar wind and the heliospheric magnetic field (HMF). The cyclic nature of the Sun's global magnetic field together with transient solar eruptions are responsible for a time-dependent variation in GCRs, at the Earth, with particle rigidities below ~ 30 GV (Strauss & Potgieter 2014). The large-scale modulation pattern of GCRs affected by the Sun follows closely the 11-year solar cycle (Cliver et al. 2013; Usoskin 2023). For shorter-term fluctuations to GCR fluxes in the heliosphere, one important influence is *solar activity*, i.e. magnetic phenomena in interplanetary space whose origin is the Sun. Typically, such fluctuations range from the order of a few days to the period of a solar rotation (Cane 2000).

Aguilar et al. (2021) report GCR proton observations measured by the *Alpha Magnetic Spectrometer 02* (AMS-02; Battiston 2008; Ting 2013), located on the International Space Station, that show a large and long depression, between 3-4 Bartel rotations (BRs), at lower rigidity, during the second half of 2017. This depression spans about one fifth of the overall solar cycle variation. Such a large variation was unexpected at that time as solar activity was progressing towards the minimum of Solar Cycle 24. In Figure 1, the top panel shows the variation of Bartel rotations-averaged galactic proton observations of rigidity 1.0 - 1.16 GV, from BRs 2474 - 2540, 01 December 2014 - 29 October 2019, reported by Aguilar et al. (2021). The left scale indicates the proton flux and the right scale is the normalized flux with respect to BR 2508, 06 June - 03 July 2017, when the depression initiates. The bottom panel of Figure 1 shows the variation of neutron monitor (NM) counts recorded by the Oulu NM for the same period of BRs 2474 - 2540. The

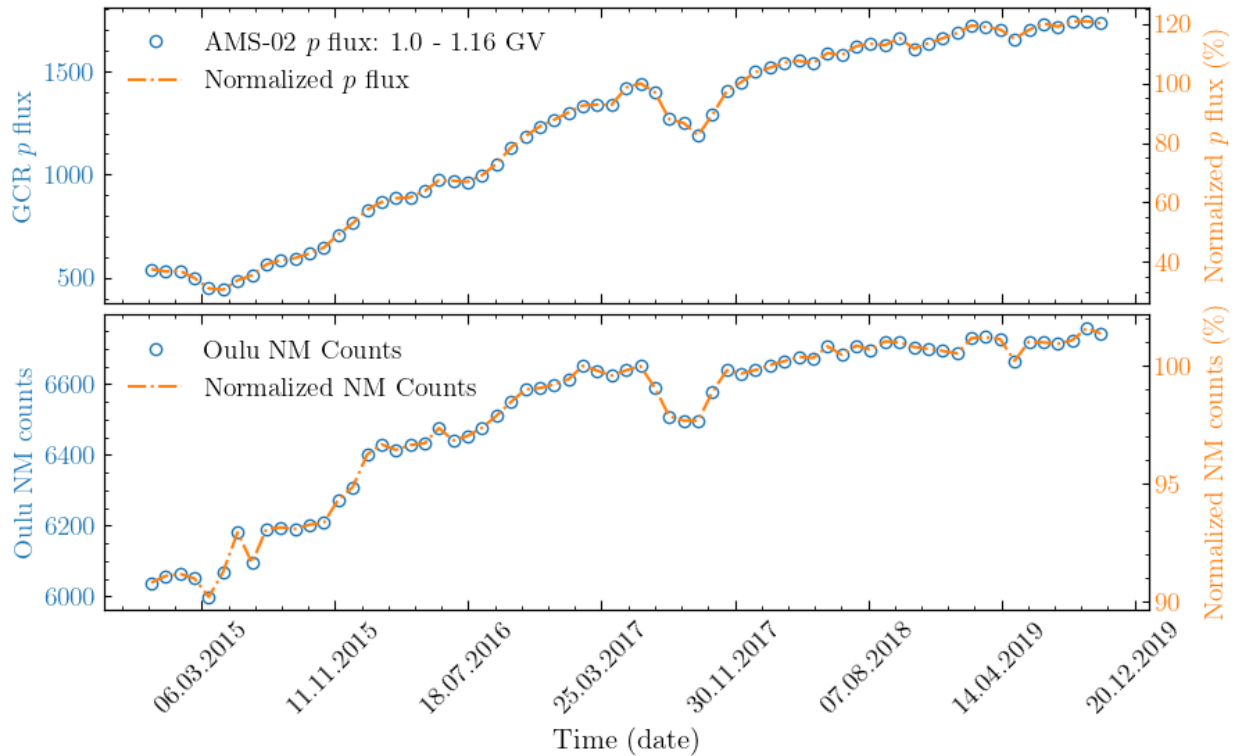


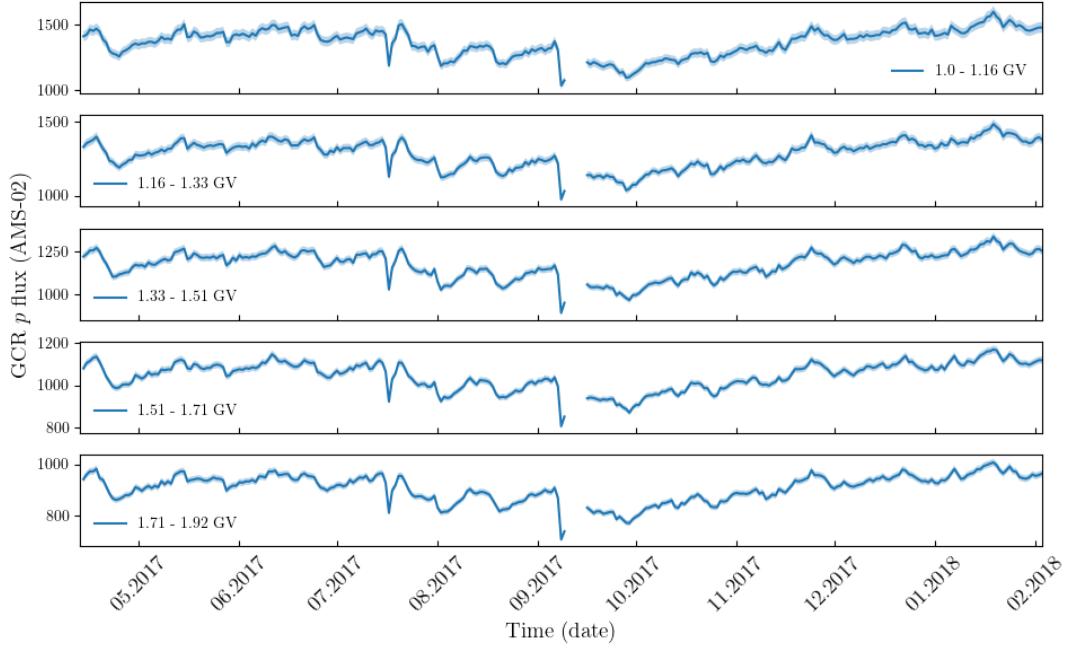
Figure 1. Top: Bartel rotations-averaged galactic proton flux variation over the rigidity 1.0 -1.16 GV from 01 December 2014 (BR2474) to 29 October 2019 (BR2540), reported by Aguilar et al. (2021). Bottom: Same resolution neutron monitor counts recorded by Oulu neutron monitor for the same time period. Left scale shows the flux or NM counts, and the right scale indicates the normalized flux or counts with respect to BR2508.

left scale indicates the NM counts per minute and the right scale displays the normalized counts with respect to BR 2508. The AMS-02 measurements of GCR proton flux show a decrease of 17.43% within 4 BRs, which, as mentioned above, is almost one fifth of the overall variation (90.22%) reported from the December 2014 - October 2019 period, in the rigidity bin 1.0 - 1.16 GV. This variation is mirrored in the depression observed in the NM counts, where although the decrease is 2.32%, this represents $\sim 20\%$ of the overall variation from December 2014 - October 2019 (and 11.41% from solar maximum to minimum).

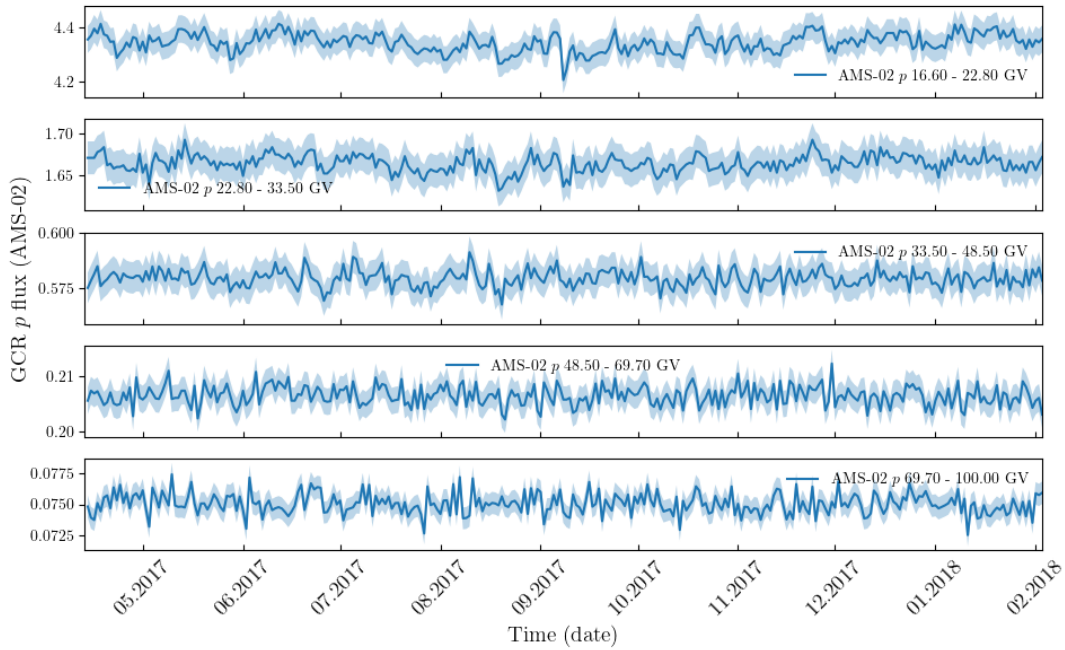
The presence of a large depression in the proton flux lasting for almost half a year, while solar minimum is being approached, is an unusual signature that is too large to be explained by any individual solar-eruptive event. The purpose of this work is to determine the cause of this depression and we do this by investigating two approaches. First, we consider a possible large-scale change to the HMF due to a change in the behaviour of the Sun’s global magnetic field. Secondly, we consider the effect of a combination of different solar activity events that potentially act together to produce a larger effect than any individual solar-eruptive event. The rest of the paper is outlined as follows: our two approaches of investigation are described in detail. We then perform a detailed investigation of observational data related to each approach. Based on the observational evidence, we evaluate both approaches, and the paper concludes with a discussion of the results.

2. POSSIBILITIES: LONG-TERM OR TRANSIENT STRUCTURES

As stated above, the observed depression in Figure 1 is too large to be attributed to any individual solar-eruptive event. Such a statement presupposes that the Sun is the origin of the depression, but this needs to be confirmed. To do this, we consider the daily proton flux from AMS-02 (Aguilar et al. 2021), for the period in question, over a range of rigidity bins. If the main cause were due to some extra-heliospheric phenomenon, it would be expected that similar signatures would be observed in both high and low rigidity bins. If the origin of the depression were solar, however, then only the lower rigidities would be expected to carry the signature. Figure 2 displays the daily proton fluxes from AMS-02 for (a) low and (b) high rigidity bins. By comparing the panels in Figure 2 (a) and (b), it is clear that the



(a)



(b)

Figure 2. Daily galactic proton observations measured by AMS-02 for the 13 April 2017 - 03 February 2018 (BR 2506 - 2516) as reported by Aguilar et al. (2021), over (a) the first five rigidity bins, 1.0 - 1.16 GV, 1.16 - 1.33 GV, 1.33 - 1.51 GV, 1.51 - 1.71 GV & 1.71 - 1.92 GV, and (b) the last five rigidity bins 16.60 - 22.80 GV, 22.80 - 33.50 GV, 33.50 - 48.50 GV, 48.50 - 69.70 GV & 69.70 - 100.00 GV. The shading indicates the total error in GCR proton flux as reported.

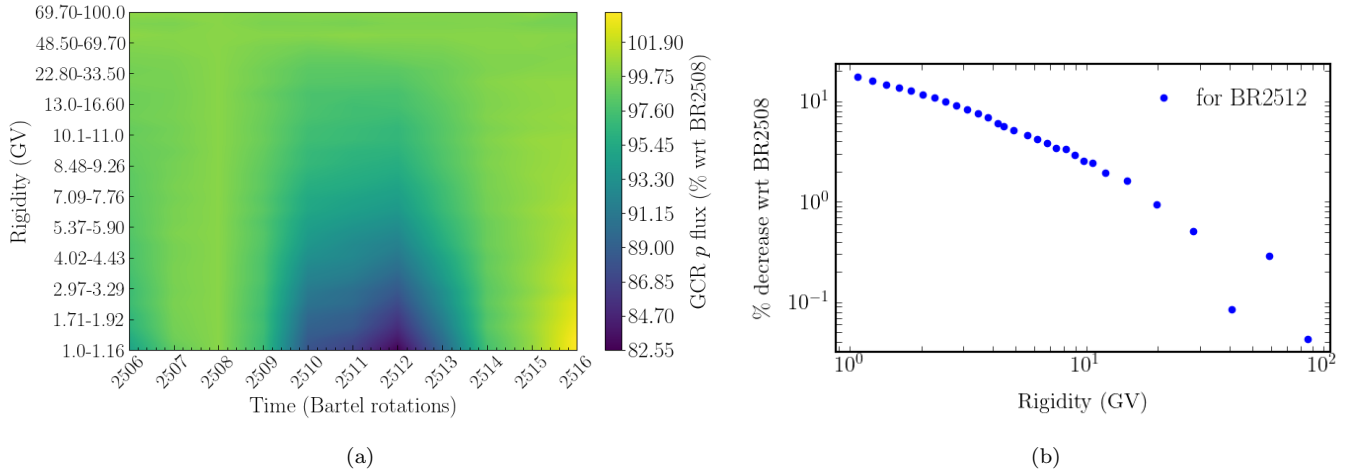


Figure 3. (a) Normalized BR-averaged GCR proton flux variation from BR2506 to BR2516 over the rigidity bins 1.0 -1.16 GV to 69.7-100.0 GV. Flux is normalized with respect to the BR2508. (b) The % decrease in flux at BR2512 with respect to BR2508 over rigidity bins up to 100.0GV.

consistent signature for low rigidities is lost at higher rigidities. This result is also conveyed in Figure 3 (a), which displays a heat map for the normalized proton depression for many rigidity bins across the Bartel rotations covering the event. Figure 3 (b) shows that the normalized decrease varies across rigidity for Bartel rotation 2512, when the minimum occurred. These figures indicate that the signature of the depression begins to weaken for rigidities $\gtrsim 30$ GV, which is in line with values quoted in the literature (Potgieter 2017). Thus, we attribute a solar origin to the GCR depression.

With the data indicating a solar origin, two possible explanations for the origin of the depression need to be considered. The first is that, rather than solar activity being the primary cause, medium to long-term modulation effects, such as the observed depression, are functions of changes in the Sun’s global magnetic field. Such an effect is referred to as a *minicycle* (Garcia-Munoz et al. 1977; Wibberenz & Cane 2000), and is the first possibility for the observed depression that we will discuss. The second possibility that we consider is that the source of the observed depression lies primarily in solar activity. By *activity*, we refer primarily to *coronal mass ejections* (CMEs) and *interaction regions* (IRs), that will be described in more detail later. We will investigate if a combination of CMEs and IRs can create the observed depression. We now describe each of the two possibilities in more detail.

2.1. The Minicycle

In 1974, a year-long modulation event occurred, near to solar minimum, that was qualitatively similar to the half-year-long observed depression of this study (Garcia-Munoz et al. 1977; Cliver et al. 1993; Wibberenz & Cane 2000; Wibberenz et al. 2001). This event has been named the *1974 minicycle* and it has been argued that its origin is due to a change in the Sun’s global magnetic field and not transient solar-eruptive effects (Tsurutani et al. 1995; Wibberenz & Cane 2000). There are several key characteristics that define the 1974 minicycle. The observed depression for this event, detected in Mount Wellington NM data, mirrors very closely an increase in the magnitude B of the HMF. This period is also matched closely by an increase in the tilt angle of the solar dipole, with a maximal change of almost 30° during this period. Wibberenz & Cane (2000) argue that these changes in the solar magnetic field are the cause of the observed modulation event due to the absence of any enhanced CME activity. With its qualitative similarity to the observed depression of 2017, we test the minicycle hypothesis as a possible source of the observed depression. To do this, we will investigate the behaviour of B and the tilt angle and evaluate their effects relative to any strong solar activity.

2.2. CMEs and IRs

Amongst the plethora of solar-eruptive phenomena, it is the large-scale structures of CMEs and IRs that are considered to play the most prominent roles in GCR modulation (Cane 2000; Modzelewska et al. 2020; Dumbović et al. 2020, 2022; Guo et al. 2024). CMEs originate in the solar atmosphere and take the form of magnetic flux ropes

that are ejected into space. The expansion of these ropes (also referred to as magnetic clouds) with increasing radial distance from the Sun provides a ‘magnetic obstacle’ for low-rigidity GCRs. The classical signature of CME-induced modulation is the *Forbush Decrease* (FD) [Forbush \(1937\)](#). Although the shape of a FD is qualitatively similar to the BR-averaged 2017 observed depression, the duration of a FD is of the order of a few days and not half a year. Thus, not one but many CMEs would be required to produce a combined effect long enough to span the observed dip. The merging of several CMEs beyond the Earth, forming Global Merged Interaction Regions (GMIRs), has long been studied ([Burlaga et al. 1993](#)). At these large distances, the CMEs have expanded to become much larger than at 1 AU, thus having a form to create a longer-lasting modulation event. At 1 AU, it remains to be seen if a sequence of CMEs (near solar minimum) is enough to produce a GMIR-like effect that is sufficient enough to create the observed dip.

In addition to CMEs, there is also the presence of IRs. IRs are formed when the fast solar wind, from coronal holes, catches up with the ambient slow solar wind. The result is a compression of plasma in this interacting region followed by a rarefaction in the fast solar wind ([Gosling & Pizzo 1999](#)). Such events are referred to as *stream interaction regions* (SIRs). Due to the longevity of some coronal holes, SIRs may persist for several rotations. In this case, they are referred to as *corotating interaction regions* (CIRs) in the literature. CIRs are known to produce FD-like depressions, which can be longer-lived than those due to CMEs but are typically weaker in magnitude ([Modzelewska et al. 2020](#); [Dumbović et al. 2022](#); [Romaneehsen et al. 2024](#); [Guo et al. 2024](#)). In the context of modelling the features of CIRs on GCR modulation, see e.g. [Kopp et al. \(2017\)](#); [Luo et al. \(2020, 2024\)](#).

In order to determine whether or not solar activity is the primary cause of the observed depression, a record of CMEs and IRs during this period needs to be made. The contributions of these events then need to be identified in the GCR proton flux time series to confirm that the combined effects of individual events lead to the prolonged existence of the observed depression.

2.3. Possibility of a minicycle

In order to test the possibility of a minicycle, we must seek the key characteristics reported by [Wibberenz & Cane \(2000\)](#) for the 1974 minicycle. The main observations are an increase in the HMF field strength B with a co-temporal change in the tilt angle of the solar dipole. Further, according to the description of the 1974 minicycle, both of these signatures must occur without an enhancement of CME activity. For the 1974 minicycle, B increased by ~ 1.5 nT and the tilt angle by $\sim 30^\circ$. For the period of the observed depression under study, the key observations are displayed in [Figure 4](#).

In [Figure 4 \(a\)](#), the time variations, on a BR resolution, for the HMF magnitude B (obtained from the Advanced Composition Explorer ([Stone et al. 1998](#)) through the [OMNIWeb Plus Service](#)) and the heliospheric current sheet (HCS) tilt angle (obtained from the [Wilcox Solar Observatory](#)) are displayed. To compare with these trends, the sunspot number (SSN), obtained through the [OMNIWeb Plus Service](#) ([Simpson 2000](#)), and $F_{10.7}$ radio flux (obtained from the [Dominion Radio Astrophysical Observatory](#)) are displayed in [Figure 4 \(b\)](#), and the proton flux from AMS-02, for the rigidity bin 1.0-1.16 GV, is shown in [Figure 4 \(c\)](#). From the period starting at the end of 2016 and ending near the start of May 2017, there is an increase in B of ~ 1 nT and a decrease in the HCS tilt angle of $\sim 10^\circ$. Although smaller than the changes for the 1974 minicycle, these values are indicative of the possibility of a minicycle. Further corroboration can be found in [Figure 4 \(b\)](#) by comparing the proxies of solar activity, SSN and $F_{10.7}$, for this period. There is little variation in both quantities, particularly during the main peak in B in May 2017, and this is suggestive of no enhancement in solar eruptive activity. Further supportive evidence can be found by looking at the flares in this period. In [Appendix A](#), a list of all active regions from the end of 2016 until the start of 2018 (covering the period of the graphs in [Figure 4](#)) is presented. From the end of 2016 until the start of June 2017, there were only eight M-class flares (all pertaining to AR12644). All other flares during this period were C-class and below. Since the M-class flares occurred in the period from March 27th to April 5th 2017, it is unlikely that this activity was responsible for the peak in B , which occurred almost one month later.

Until now, the evidence has been pointing in the direction of a possible minicycle. However, upon inspection of [Figure 4 \(c\)](#), the peak in B and the local minimum in the HCS tilt angle are approximately co-temporal with a local maximum in the proton flux. This observation differs from that of the 1974 minicycle, in which there were already significant dips in proton and NM data when B was at its maximum. It is only by the start of June 2017, after the peak activities of B and the HCS tilt angle, that we find the observed depression in the GCR data. This behaviour corresponds to another increase in B and decrease in the HCS tilt angle. The situation, however, is different from

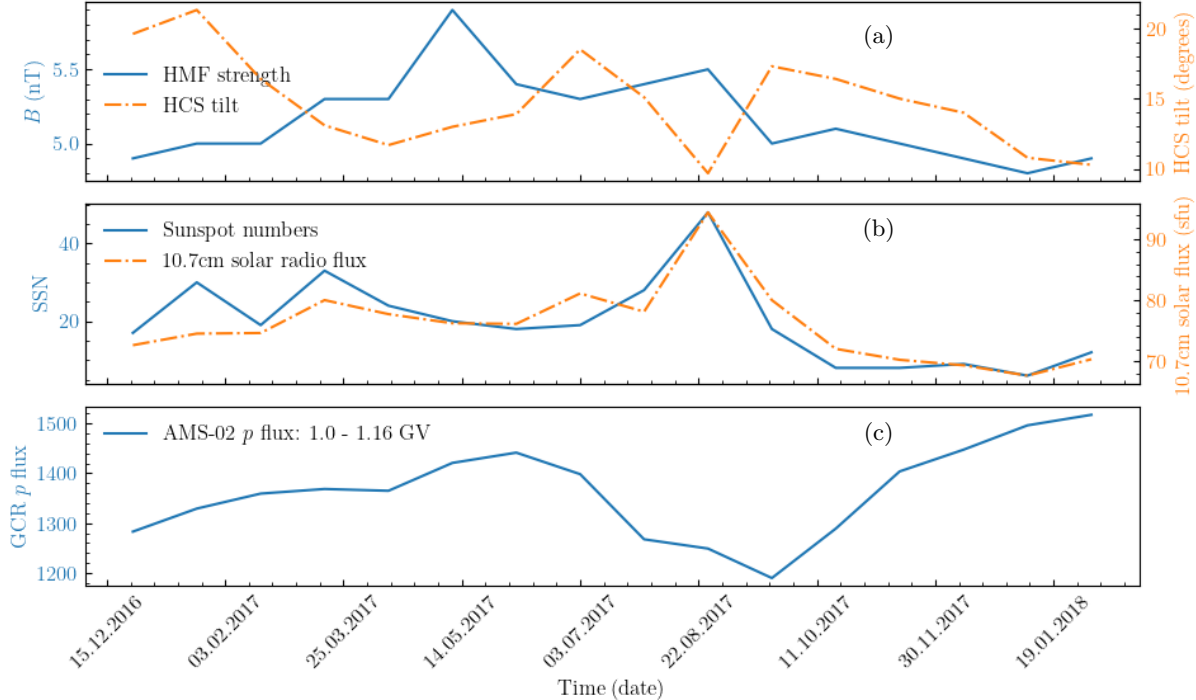


Figure 4. Time variation over a BR resolution of, top: IMF strength (blue) & HCS tilt angle (orange), middle: sunspot numbers (blue) & 10.7cm solar radio flux (orange) and bottom: GCR proton flux in the rigidity bin 1.0-1.16 GV, for 26 December 2016 to 03 February 2018 period.

before. There are now large peaks in the SSN and $F_{10.7}$ data co-temporal with the peak in B and the minimum in the HCS tilt. This information suggests that there is an increase in solar eruptive activity contributing to both the changes in B , the HCS tilt angle and the proton flux. From mid-August to mid-September 2017, there was a group of highly eruptive active regions (AR12671 - AR12674) that were responsible for the peaks in Figure 4 (b). One of these regions, AR12673, also produced four X-class flares, including the strongest flare of the solar cycle (Hou et al. 2018; Lei et al. 2020; Raphaldini et al. 2023).

To summarize, while indicative minicycle signatures appeared before the observed depression, it is clear that significant enhanced eruptive activity, co-temporal with the observed depression, cannot be excluded. For this reason, we cannot attribute the observed depression to a minicycle, at least in the sense of the 1974 minicycle described by Wibberenz & Cane (2000). Instead, to fully reveal the origin of the observed depression, we must go to our second possibility and examine the combined effects of solar activity.

3. SOLAR ACTIVITY

3.1. General picture

To investigate how solar activity may be the cause of the observed depression, it is important to identify all the key elements (CMEs, SIRs and CIRs) that contribute to it. Before performing this in detail, it is useful to present a simplified picture of what general behaviour is expected. Such a picture is presented in Figure 5.

Figure 5 (a) displays the idealized behaviour of the GCR proton flux over two Carrington rotations as the solar cycle is approaching solar minimum. The general trend, averaged over Carrington rotations, is an increase in the proton flux. However, the “full resolution” rise is not monotonic due to solar rotation. $C(n)$ represents the n th Carrington rotation, with subsequent rotations being labelled $C(n+1)$, $C(n+2)$, etc. Within each Carrington rotation, the dip is caused by coronal holes producing CIRs. From the point of view of the impact on GCR flux, the impact of a CIR follows the rotation. Thus, instead of discussing CIRs per se, we will consider Carrington rotations as the markers of CIR impact on GCR flux. Such a choice is clear from the picture in Figure 5 (a), but it will also become clear when examining the proton flux data in detail.

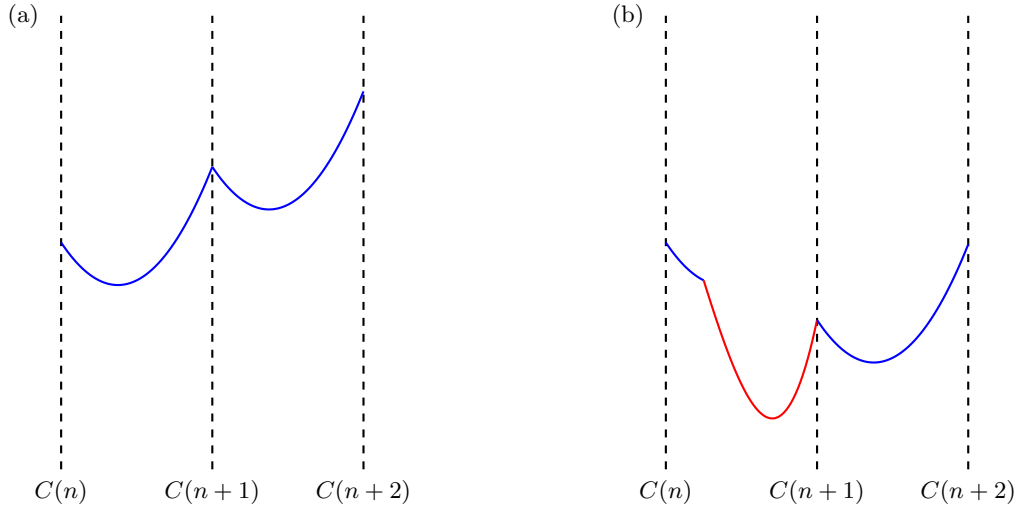


Figure 5. Idealized representations of GCR proton flux, approaching solar minimum, over two Carrington rotations, with the n th dashed line marking the start of Carrington rotation $C(n)$. (a) shows the expected behaviour due only to CIRs. (b) shows the expected behaviour due to a disturbance, e.g. a CME, during the first Carrington rotation.

In Figure 5 (b), there is a disturbance, shown in red, between $C(n)$ and $C(n+1)$. This disturbance represents the possible effect of a CME or a combination of CMEs and SIRs. In this picture, the disturbance ends at $C(n+1)$ and the proton flux in the next Carrington rotation proceeds as in Figure 5 (a). The effect of the disturbance has been to reduce the level of the proton flux at $C(n+2)$ compared to its “undisturbed” value in (a). If many such disturbances occur, they may delay the rise of the proton flux and create the signatures displayed in Figures 1 and 3. We now investigate this possibility in the data.

3.2. Data analysis

Figure 6 displays the daily proton fluxes at low rigidities (bins 1 - 1.16 GV and 2.97 - 3.29 GV) over the period of the depression from 23 June to 03 December 2017. To aid the interpretation of the results, the beginnings of Carrington rotations are indicated by blue vertical lines and are labelled above.

This figure will provide a reference point for the description of solar activity. In addition to this figure, Table 1 displays the start and end times of the Carrington rotations (CIRs) and major SIRs and CMEs relevant for the period. The strengths of the flares associated with each CME are also displayed, providing a relative indicator of the amount of energy released, together with their positions of origin on the solar surface and associated active region numbers. Finally, the % decrease of proton flux associated with each event, as seen in Figure 6, is displayed.

All of the data for Table 1 have been collected from online catalogues for a range of instruments. For data of CME arrival times at 1 AU, there are the resources of Richardson & Cane (Cane & Richardson 2003; Richardson & Cane 2010), HELIO4CAST (Möstl et al. 2020), WIND data from DREAMS (Chi et al. 2016) and STEREO (Jian et al. 2018). Carrington rotation (CIR) times and labels can be obtained from the Wilcox Solar Observatory and SIR times are available from STEREO (Jian et al. 2019). Flare strengths and active region locations on the solar surface can be obtained from SolarMonitor (Gallagher et al. 2002).

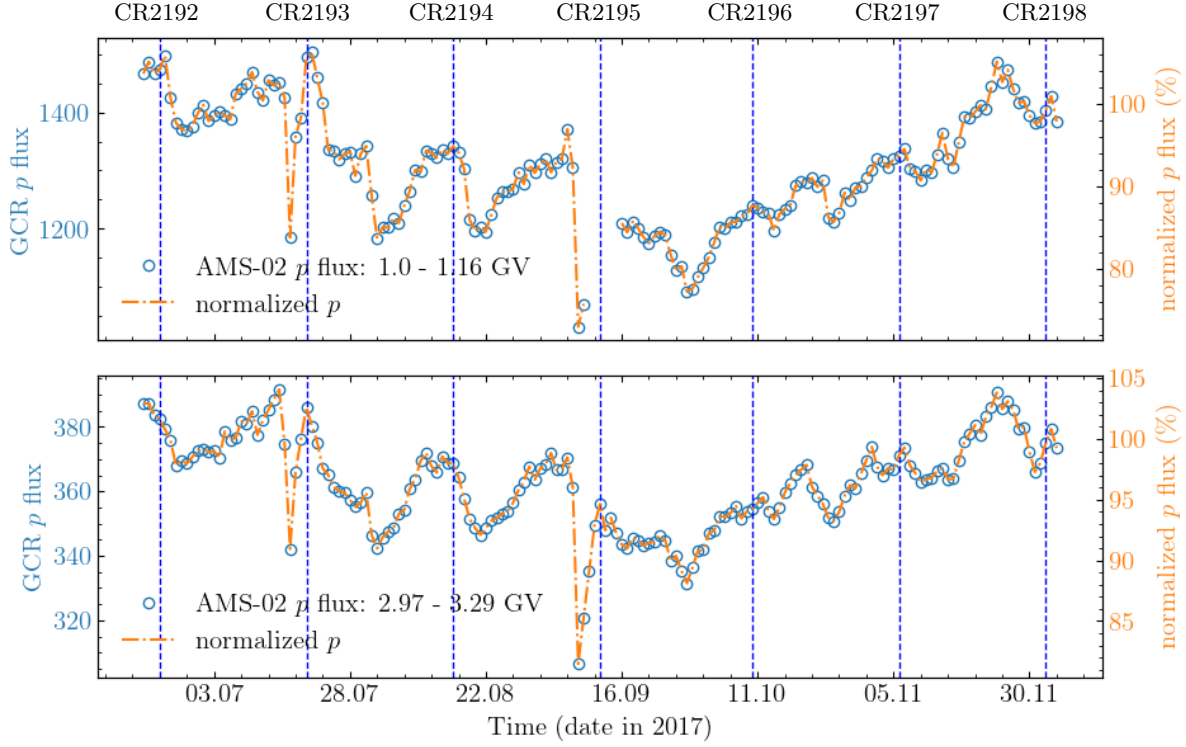


Figure 6. AMS-02 reported daily resolution GCR protons from 20 June to 05 December, 2017 at 1.0 - 1.16 GV (upper panel) and 2.97 - 3.29 GV (lower panel). The left scale is proton flux and right scale is normalized flux with respect to 06 June, 2017. The vertical blue lines indicate the beginnings of the Carrington rotations during this period. During the 09 - 15 September, 2017, daily proton AMS-02 measurements were not available below the 2.97- 3.29 GV rigidity bin.

Table 1. Identified solar activity during the June - December (CR2192 - CR2197) 2017 period (times correspond to activity at 1 AU). The GCR % decrease is for the rigidity bin 1.0-1.16 GV. Generative active regions and locations on the solar surface are displayed for CMEs, together with associated flare strengths.

Start	End	Structure	Region, location	Flare strength	% dec.
23-06T00:00	20-07T07:00	CR2192	–	–	9.25
23-06T03:00	25-06T22:00	SIR	–	–	–
01-07T00:00	02-07T00:00	SIR	–	–	2.02
04-07T02:53	06-07T09:14	CME	AR12664, N18W85	B	0.83
04-07T04:00	06-07T04:00	SIR	–	–	–
09-07T01:00	10-07T01:00	SIR	–	–	3.39
11-07T04:00	14-07T04:00	SIR	–	–	–
15-07T12:00	16-07T12:00	CME	AR12667, N11W68	C8.4	–
16-07T05:10	17-07T20:00	CME	AR12665, S09W33	M2.4	18.99
16-07T14:00	18-07T12:00	SIR	–	–	–
19-07T19:00	21-07T22:00	SIR	–	–	–
20-07T07:00	16-08T13:00	CR2193	–	–	11.97
24-07T14:35	27-07T11:00	CME	AR12665, S06W89	C1.3	1.10
25-07T05:43	27-07T10:49	CME	–	B	3.0
29-07T22:50	31-07T22:53	CME	–	B	11.31
08-08T12:00	09-08T21:00	SIR	–	–	–

16-08T13:00	12-09T20:00	CR2194	–	–	10.56
17-08T00:00	21-08T14:00	SIR	–	–	–
21-08T22:00	23-08T18:00	CME	AR12671, N11E08	C	0.70
23-08T01:00	25-08T20:00	SIR	–	–	–
28-08T20:00	30-08T06:00	SIR	–	–	1.24
31-08T21:00	02-09T00:00	CME	–	–	1.06
03-09T21:00	06-09T00:00	SIR	–	–	1.47
06-09T23:02	08-09T04:00	CME	AR12673, S11W16	M5.5	–
07-09T22:28	10-09T21:00	CME	AR12673, S08W33	X9.3	24.4
12-09T20:00	10-10T03:00	CR2195	–	–	–
13-09T16:50	14-09T18:00	SIR	–	–	–
18-09T13:17	19-09T00:00	SIR	–	–	–
19-09T02:56	21-09T09:30	CME	AR12680, N08W25	B	2.57
25-09T14:00	29-09T12:00	SIR	–	–	4.40
30-09T12:00	04-10T18:00	SIR	–	–	–
10-10T03:00	06-11T09:00	CR2196	–	–	3.18
10-10T19:30	12-10T06:35	SIR	–	–	–
15-10T07:49	15-10T22:47	SIR	–	–	–
21-10T03:24	23-10T06:58	CME	AR12684, N11W74	B	1.06
24-10T08:36	25-10T06:58	CME	AR12685, S12E88	M1.1	5.04
28-10T12:00	31-10T20:00	SIR	–	–	–
05-11T07:00	06-11T16:00	SIR	–	–	–
06-11T09:00	03-12T16:00	CR2197	–	–	3.95
11-11T20:00	15-11T16:00	SIR	–	–	–
14-11T01:08	14-11T14:13	CME	AR12687, S08E52	B	0.42
15-11T11:47	15-11T19:23	CME	AR12687, S08E52	B	4.22
17-11T00:00	17-11T21:53	SIR	–	–	–
19-11T18:00	22-11T12:00	SIR	–	–	–
23-11T20:00	25-11T07:00	SIR	–	–	2.57
01-12T18:00	03-12T18:00	SIR	–	–	–

After the onset of the first Carrington rotation, CR2192, on 23 June, the proton flux reduced by almost 10% before beginning to rise. This behaviour is qualitatively similar to that described in Figure 5 (a). The rise is impeded, however, by the impact of SIRs and a CME associated with a weak B-class flare. Each of these structures causes relatively small depressions. The rise of the proton flux is halted suddenly close to the start of the next Carrington rotation by the impact of two stronger CMEs (with related C-class and M-class flares). The first, from AR12667, arrived on 16 July and the second, from AR12665, on 17 July. The combined effect of these two CMEs was to produce a depression of almost 19%.

Although the proton flux at the start of CR2193 is at a similar level to that at the start of CR2192, its value is lower than it would have been had there not been the significant impact of the CMEs. The proton flux in the next two Carrington rotations behaves in a qualitatively similar manner compared to that of CR2193 - a CIR-related decrease at the start of the rotation followed by large impacts due to CMEs. The largest impact occurs near the end of CR2194 and is due to the combination of two CMEs associated with the strongest flares during this period. Indeed, the second of these CMEs is associated with the strongest flare of the entire solar cycle. Figure 7 displays the combined effect of these CMEs in higher-resolution NM data.

It is clear from Figure 7 that the recovery from the first CME impact is interrupted by the arrival of the second, which further prolongs the depression. Other features (CR2195 and an SIR) from available catalogues, that are listed in Table 1, are also labelled in this figure. Although there are CMEs in the remaining Carrington rotations of the depression, their relative impacts become smaller until, by CR2198, the proton flux begins to go “back on track” and follow the general rise expected as the solar cycle proceeds to its minimum.

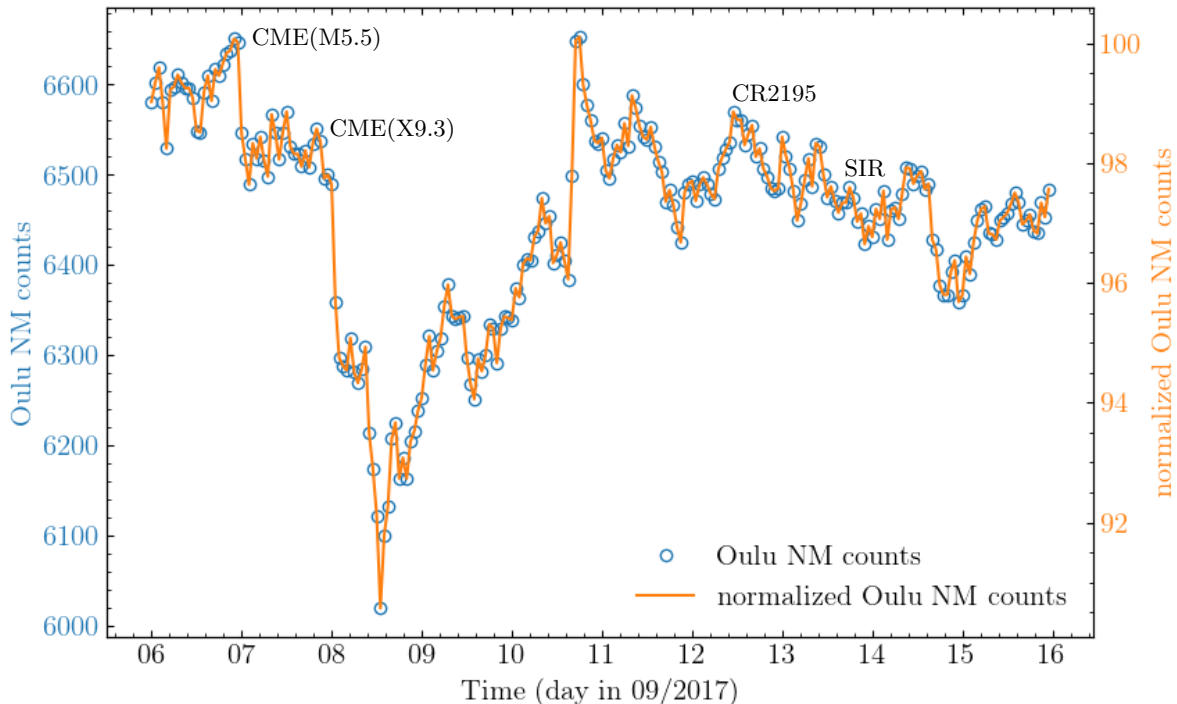


Figure 7. Oulu NM data covering the impact of the two strongest flares during the depression. Other features from Table 1 are also indicated.

While the combination of various CMEs and SIRs in each Carrington rotation help to keep the proton flux lower than in “quiet” heliospheric conditions, the largest impacts come from CMEs associated with M-class and X-class flares. These CMEs are from AR12665, AR12673 and AR12685, and what is particular about them is that they all correspond to the same magnetic source, with different labels for different solar rotations. This particular magnetic source actually existed for five Carrington rotations and represents a localized region of the Sun in which complex magnetic field continued to emerge into the atmosphere and provide the energy required to produce the strong observed flares and CMEs. Thus, the main driver of this half-year depression in the proton flux has as its source, one highly-eruptive and evolving magnetic region (the most active of Solar Cycle 24).

3.3. Effect across rigidities

So far, our focus has been on protons with low rigidities in the 1 - 1.16 GV and 2.97 - 3.29 GV bins. However, as indicated in Figure 3, the depression can still be detected clearly for rigidities up approximately 30 GV. We now show how individual impacts behave across different rigidities. Figure 8 displays information about how the % decrease (normalized with respect to the value from 06 June) depends on rigidity for two periods covering 20 June to 01 August and 14 August to 25 September.

Figure 8 (a) shows a heat map of how the % decrease behaves for rigidities in the range 1 - 100 GV over time. This period covers CR2192 and part of CR2193. The first strong CME on 17 July can be seen with a clear signature up to the 22.80 - 33.50 GV bin. The initial depressions at the start of Carrington rotations (CIRs) as well as SIRs are also clearly visible up to rigidities of around 30 GV. Figure 8 (b) displays the % decrease during the depression of the first CIR shown in (a) and the main CME. This plot reveals that the % decreases, for both the CME and the CIR, appear to follow power laws closely up to ~ 30 GV. After this point, there is more scatter.

Figures 8 (c) and (d), covering CR2194 and part of CR2195, show similar properties to those in (a) and (b), despite the missing data from 09 to 15 September. Again, for this period, we see a clear power law-dependence of the % decrease with rigidity up to ~ 30 GV.

4. SUMMARY AND DISCUSSION

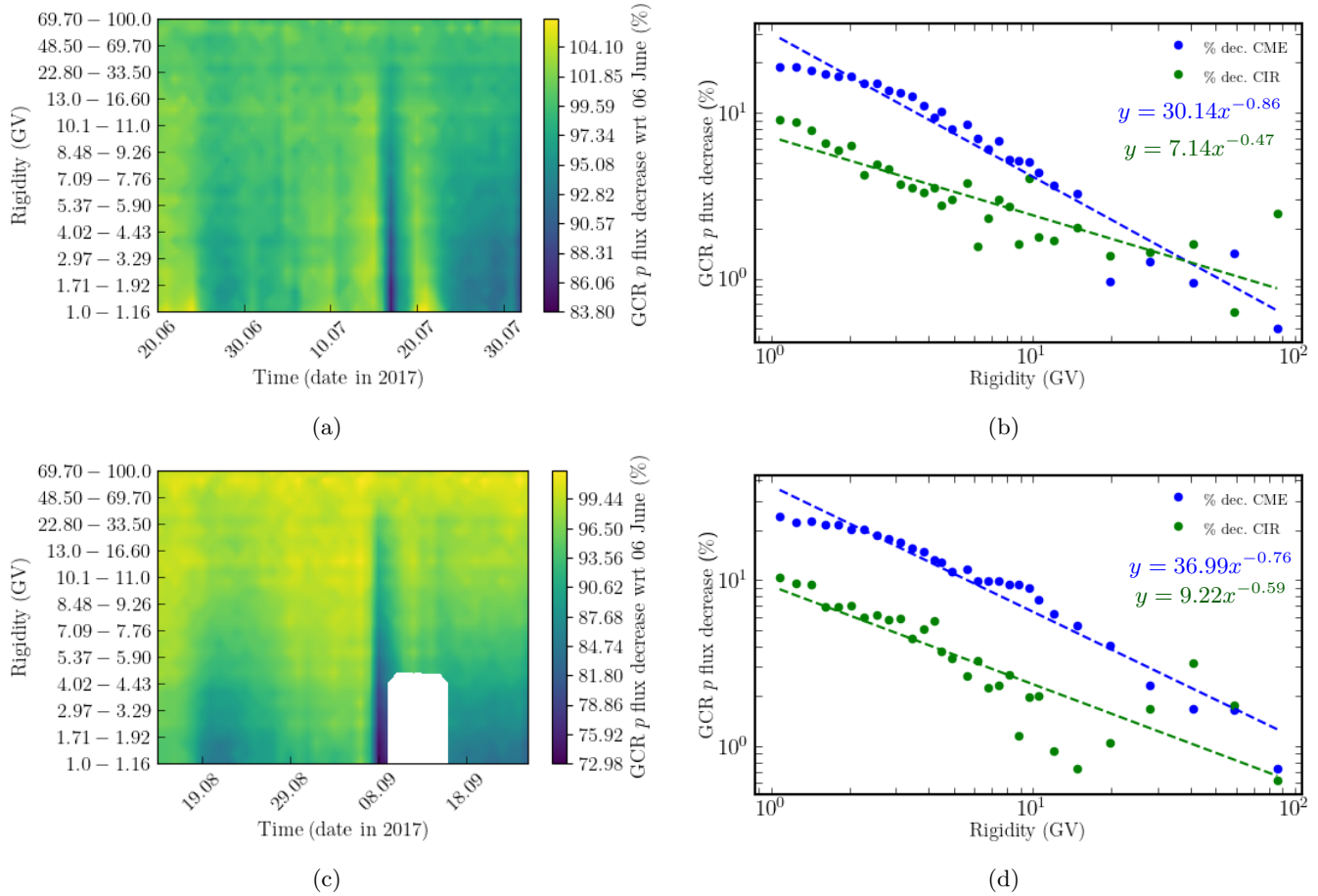


Figure 8. Daily GCR proton flux reported by [Aguilar et al. \(2021\)](#), normalized with respect to 06 June, 2017, over the whole reported rigidity range 1.0 - 100.0 GV, (a) for 20 June - 01 August, 2017 including CR2192 and (c) 14 August - 25 September, 2017 including CR2194. Note that for 09 - 15 September, below 2.97 - 3.29 GV, the proton flux data are missing. Both heat maps reveal CIRs (thick and dark vertical bands), SIRs (weak, thin and dark vertical bands) and CMEs (strong, thin and dark vertical bands). (b) and (d) show the % decrease as a function of rigidity for the first CIR and CME from (a) and (c) respectively. Power law fits are included to indicate the clear trends for lower rigidity particles. The formulae of the power laws are also indicated.

In this work, we have investigated the source of an unexpectedly long depression in the GCR proton flux, reported by [Aguilar et al. \(2021\)](#), lasting the second half of 2017. To achieve this task, we first identified the depression as being of solar origin. We then considered two possible sources for the depression - a minicycle due to a change in the global solar magnetic field, and a combined effect due to solar activity in the form of CIRs, SIRs and CMEs. After comparing the global properties of the HMF strength and the HCS tilt to the behaviour of the 1974 minicycle ([Wibberenz & Cane 2000](#)), it was shown that the presence of some strong erupting active regions could not be ignored. Thus, in order to evaluate the how solar activity was connected to the depression, we identified all the catalogued CIRs and major SIRs and CMEs during this period. The proton flux depression lasted for five Carrington rotations, and we identified key features in each rotation. First, each Carrington rotation began, as expected, with an initial decrease in the proton flux. The subsequent rise was then impeded by a combination of CMEs and SIRs, and this general picture holds for each Carrington rotation although the relative decreases in the proton flux weakened by the final rotation. As part of this combination of different effects, four strong CMEs related to M-class or X-class flares, occurring in different Carrington rotations, caused the largest impacts. What is particular here is that all of these CMEs came from the same magnetic source, which perpetuated for five Carrington rotations. One phase of this magnetic source, when it was labelled AR12673, produced the strongest flare of the entire solar cycle ([Hou et al. 2018](#)). Therefore, from our findings, we conclude that the half-year depression observed in the GCR proton flux was caused by a combination

of CIRs, SIRs and CMEs but was enhanced substantially due to strong CMEs emanating from an unusually active magnetic source (indeed, the most active of the cycle). We say “unusually active” because the phase of the solar cycle was approaching solar minimum. It is also for this reason, that the depression is more visible - it reverses the trend of the global proton flux rise (see Figure 1), whereas if the depression were in a phase approaching solar maximum, the depression would be in the same general direction as the global trend.

Although we excluded a minicycle as being the primary cause of the depression, this was based on the definition of the 1974 minicycle, for which there was no enhanced CME activity (Tsurutani et al. 1995). To our knowledge, within the field of solar dynamo theory, very little attention has been afforded to minicycles. Although in some works, minicycle-like features seem to appear (e.g. Figure 4 of Busse & Simitev 2011), they have not been treated as an object of study in their own right. In our situation, we have some evidence of behaviour like the 1974 minicycle before the depression, but the difference is that there is a clear link between the depression and intense CME activity. However, we cannot exclude the possibility of a minicycle with a broader definition than the 1974 minicycle. Since all magnetic activity on the Sun ultimately derives from its dynamo, there must be some process that has led to the creation of the most eruptive active region as the solar cycle approaches its minimum. This may be another form of a minicycle which we suggest would be an interesting area of research in the future.

In this work, our main focus has been on the proton flux. In a follow-up to this work, we will model the modulation, (Potgieter 2013; Potgieter et al. 2014, 2021) of protons and other GCRs, including helium (Ngobeni et al. 2020), electrons and positrons (Aslam et al. 2021), making use of AMS-02 data for these species (Aguilar et al. 2021, 2022, 2023a,b). This study will also help to explore the behaviour of particles with rigidities below 1 GV, for which observations are not currently available for the period under investigation. Further, we will also be able to simulate the modulation of anti-protons (e.g. Aslam et al. 2023) for this period, and compare this to the modulation of protons in order to study charge-sign dependence for this particular type of event.

It is a pleasure to thank Paolo Zuccon for helpful discussions. O.P.M.A. and D.M. acknowledge support from a Leverhulme Trust grant (RPG-2023-182). D.M. also acknowledges support from a Science and Technologies Facilities Council (STFC) grant (ST/Y001672/1) and a Personal Fellowship from the Royal Society of Edinburgh (ID: 4282).

REFERENCES

- Aguilar, M., Cavazonza, L. A., Ambrosi, G., et al. 2021, *PhRvL*, 127, 271102
- . 2022, *PhRvL*, 128, 231102
- . 2023a, *PhRvL*, 130, 161001
- Aguilar, M., Ambrosi, G., Anderson, H., et al. 2023b, *PhRvL*, 131, 151002
- Alielden, K., MacTaggart, D., Ming, Q., Prior, C., & Raphaldini, B. 2023, *RAS Techniques and Instruments*, 2, 398
- Aslam, O. P. M., Bisschoff, D., Ngobeni, M. D., et al. 2021, *ApJ*, 909, 215
- Aslam, O. P. M., Potgieter, M. S., Luo, X., & Ngobeni, M. D. 2023, *ApJ*, 953, 101
- Battiston, R. 2008, *Nuclear Instruments and Methods in Physics Research A*, 588, 227
- Burlaga, L. F., McDonald, F. B., & Ness, N. F. 1993, *J. Geophys. Res.*, 98, 1
- Busse, F., & Simitev, R. 2011, *Geophysical and Astrophysical Fluid Dynamics*, 105, 234
- Cane, H. V. 2000, *SSRv*, 93, 55
- Cane, H. V., & Richardson, I. G. 2003, *Journal of Geophysical Research (Space Physics)*, 108, 1156
- Chi, Y., Shen, C., Wang, Y., et al. 2016, *SoPh*, 291, 2419
- Cliver, E. W., Droege, W., & Mueller-Mellin, R. 1993, *J. Geophys. Res.*, 98, 15231
- Cliver, E. W., Richardson, I. G., & Ling, A. G. 2013, *SSRv*, 176, 3
- Dumbović, M., Vršnak, B., Temmer, M., Heber, B., & Kühl, P. 2022, *A&A*, 658, A187
- Dumbović, M., Vršnak, B., Guo, J., et al. 2020, *SoPh*, 295, 104
- Forbush, S. E. 1937, *Physical Review*, 51, 1108
- Gallagher, P. T., Moon, Y. J., & Wang, H. 2002, *SoPh*, 209, 171
- Garcia-Munoz, M., Mason, G. M., & Simpson, J. A. 1977, *ApJ*, 213, 263
- Gosling, J. T., & Pizzo, V. J. 1999, *SSRv*, 89, 21
- Guo, J., Wang, B., Whitman, K., et al. 2024, *Adv. Space Res.*, inpress
- Hoeksema, J. T., Liu, Y., Hayashi, K., et al. 2014, *SoPh*, 289, 3483
- Hou, Y. J., Zhang, J., Li, T., Yang, S. H., & Li, X. H. 2018, *A&A*, 619, A100

- Jian, L. K., Luhmann, J. G., Russell, C. T., & Galvin, A. B. 2019, *SoPh*, 294, 31
- Jian, L. K., Russell, C. T., Luhmann, J. G., & Galvin, A. B. 2018, *ApJ*, 855, 114
- Kopp, A., Wiengarten, T., Fichtner, H., et al. 2017, *ApJ*, 837, 37
- Lei, W. H., Li, C., Chen, F., et al. 2020, *MNRAS*, 494, 975
- Luo, X., Potgieter, M. S., Zhang, M., & Shen, F. 2024, *ApJ*, 961, 21
- Luo, X., Zhang, M., Feng, X., et al. 2020, *ApJ*, 899, 90
- Modzelewska, R., Bazilevskaya, G. A., Boezio, M., et al. 2020, *ApJ*, 904, 3
- Möstl, C., Weiss, A. J., Bailey, R. L., et al. 2020, *ApJ*, 903, 92
- Ngobeni, M. D., Aslam, O. P. M., Bisschoff, D., et al. 2020, *Ap&SS*, 365, 182
- Potgieter, M. S. 2013, *SSRv*, 176, 165
- . 2017, *Advances in Space Research*, 60, 848
- Potgieter, M. S., Aslam, O. P. M., Bisschoff, D., & Ngobeni, D. 2021, *Physics*, 3, 1190
- Potgieter, M. S., Vos, E. E., Boezio, M., et al. 2014, *SoPh*, 289, 391
- Raphaldini, B., Dikpati, M., Norton, A. A., et al. 2023, *ApJ*, 958, 175
- Richardson, I. G., & Cane, H. V. 2010, *SoPh*, 264, 189
- Romaneehsen, L., Heber, B., & Marquardt, J. 2024, *A&A*, doi:10.1051/0004-6361/202449836
- Simpson, J. A. 2000, *SSRv*, 93, 11
- Stone, E. C., Frandsen, A. M., Mewaldt, R. A., et al. 1998, *SSRv*, 86, 1
- Strauss, R. D., & Potgieter, M. S. 2014, *Adv. Space Res.*, 53, 1015
- Ting, S. 2013, *Nuclear Physics B Proceedings Supplements*, 243, 12
- Tsurutani, B. T., Gonzalez, W. D., Gonzalez, A. L. C., et al. 1995, *J. Geophys. Res.*, 100, 21717
- Usoskin, I. G. 2023, *Living Reviews in Solar Physics*, 20, 2
- Wibberenz, G., & Cane, H. V. 2000, *J. Geophys. Res.*, 105, 18,315
- Wibberenz, G., Ferreira, S. E. S., Potgieter, M. S., & Cane, H. V. 2001, *SSRv*, 97, 373

APPENDIX

A. LIST OF SOLAR ACTIVE REGIONS BEFORE AND DURING THE GCR DEPRESSION

Here we present a list of active regions that appeared before during the depression, from 25 December 2016 to 03 February 2018. These details are needed in order to evaluate the minicycle and solar activity hypotheses discussed in this work. Beside the active region number, the corresponding Space-Weather Helioseismic and Magnetic Imager Active Region Patch (SHARP; [Hoeksema et al. 2014](#)) number is listed when available. The data of this table have been collated using the catalogues cited within the main text. In addition, the functionality of the ARTop code ([Alielden et al. 2023](#)) has been used for cross-checking details. The numbers of sunspots and sunspot area mentioned here are estimates based on the information from [HELIO](#).

Table 2. Active region and flare details covering the GCR depression. See the main text for details.

AR	SHARP	Initial time & location	End time & location	No. flares & strengths	No. spots (area)
12619	6889	2016 Dec 25, N03W79	2016 Dec 26, N03W91	–	– (–)
12621	6895	2016 Dec 27, N11W57	2016 Dec 30, N10W91	8; B	04 (30)
12622	–	2016 Dec 31, N12W71	2017 Jan 02, N11W91	–	01 (10)
12623	–	2017 Jan 02, S06W19	2017 Jan 07, S06W91	–	– (–)
12624	6898	2017 Jan 04, S08W69	2017 Jan 06, S06W91	4; B	01 (–)
12625	6910	2017 Jan 13, N03E60	2017 Jan 24, N01W89	3; B	05 (80)
12626	6910	2017 Jan 14, N08E55	2017 Jan 26, N08W91	4; B	06 (160)
12627	6922	2017 Jan 21, N05E16	2017 Jan 29, N04W90	4, 1; B, C	14 (110)
12628	6920	2017 Jan 21, N12E37	2017 Jan 30, N11W91	11, 6; B, C	9 (220)
12629	6930	2017 Jan 25, N15E47	2017 Feb 05, N16W91	22; B	8 (190)
12630	6937	2017 Jan 31, N16E42	2017 Feb 10, N16W91	–	1 (10)
12631	6938	2017 Jan 31, S04W36	2017 Feb 10, N16W91	1; B	1 (10)
12632	6939	2017 Feb 01, N14W20	2017 Feb 07, N14W91	1; B	7 (60)
12633	6942	2017 Feb 03, N14W63	2017 Feb 05, N15W90	–	3 (10)
12634	6946	2017 Feb 06, N02E58	2017 Feb 17, N03W91	8; B	5 (10)
12635	6949	2017 Feb 10, N13E01	2017 Feb 17, N13W91	15, 3; B, C	9 (110)
12636	6950	2017 Feb 16, N11E41	2017 Feb 26, N11W91	3; B	4 (20)
12637	6951	2017 Feb 20, S03E49	2017 Mar 02, S04W91	–	2 (20)
12638	6952	2017 Feb 21, N18E46	2017 Mar 04, N16W91	20, 3; B, C	10 (150)
12639	6958	2017 Feb 25, S09W46	2017 Mar 01, S08W91	–	3 (20)
12640	6957	2017 Feb 27, N11E12	2017 Mar 07, N08W91	2; B	4 (30)
12641	6961	2017 Feb 28, N15E34	2017 Mar 09, N15W89	19; B	7 (100)
12642	6961	2017 Mar 02, N14W01	2017 Mar 09, N15W91	4; B	5 (40)
12643	6967	2017 Mar 22, N09E60	2017 Apr 02, N08W91	2; B	2 (30)
12644	6972	2017 Mar 27, N12E18	2017 Apr 05, N13W91	35,25,8; B, C, M	31 (570)
12645	6975	2017 Mar 28, S09E47	2017 Apr 08, S09W91	53,32; B, C	43 (700)
12646	6974	2017 Mar 28, N06W72	2017 Mar 30, N06W91	6; B	1 (20)
12647	6981	2017 Apr 01, N11W11	2017 Mar 30, N11W91	–	4 (10)
12648	6982	2017 Apr 02, S03E60	2017 Apr 13, S03W91	2; B	8 (50)
12649	6976	2017 Apr 04, N15W70	2017 Apr 06, N14W91	–	4 (30)
12650	6983	2017 Apr 10, N08E59	2017 Apr 21, N08W91	16; B	3 (40)
12651	6986	2017 Apr 19, N12E55	2017 May 01, N13W91	28, 3; B, C	8 (150)
12652	6986	2017 Apr 21, N13E51	2017 May 01, N14W91	11, 1; B, C	6 (30)
12653	6994	2017 Apr 22, S09E64	2017 May 04, S08W91	11; B	2 (100)
12654	6999	2017 Apr 29, N10E40	2017 May 09, N11W91	7; B	7 (90)

12655	7003	2017 May 05, N13E23	2017 May 14, N16W91	9; B	6 (30)
12656	7013	2017 May 17, N12E48	2017 May 28, N11W91	1; B	3 (30)
12657	7010	2017 May 17, N07E07	2017 May 24; N07W91	2; B	2 (10)
12658	7015	2017 May 19, S08E24	2017 May 27, S07W91	1; B	4 (20)
12659	7022	2017 May 22, N14E12	2017 May 30, N13W91	31, 2; B, C	13 (240)
12660	7015	2017 May 23, S11W29	2017 May 29, S11W91	4; B	10 (12)
12661	7034	2017 Jun 01, N06E65	2017 Jun 13, N07W91	35, 16; B, C	13 (240)
12662	7045	2017 Jun 14, N12E56	2017 Jun 25, N13W91	–	3 (170)
12663	7050	2017 Jun 16, N14W14	2017 Jun 22, N14W91	12; B	7 (100)
12664	7058	2017 Jun 21, N18E58	2017 Jul 03, N18W91	12; B	10 (130)
12665	7075	2017 Jul 06, S05E64	2017 Jul 18, S06W91	79, 29, 2; B, C, M	32 (730)
12666	7081	2017 Jul 13, N13W20	2017 Jul 19, N15W91	1; B	9 (30)
12667	–	2017 Jul 13, N12W91	2017 Jul 16, N12W91	7, 4; B, C	1 (10)
12668	7090	2017 Jul 26, N03W42	2017 Jul 30, N03W91	–	2 (10)
12669	7097	2017 Jul 30, N18W39	2017 Aug 03, N18W91	–	2 (10)
12670	7100	2017 Aug 03, S05E44	2017 Aug 14, S07W91	27; B	3 (170)
12671	7107	2017 Aug 15, N11E59	2017 Aug 28, N13W91	71, 22; B, C	31 (580)
12672	7110	2017 Aug 21, N05E61	2017 Sep 02, N08W91	29, 9, 1; B, C, M	19 (300)
12673	7115	2017 Aug 30, S08E50	2017 Sep 10, S09W91	2, 55, 27, 4; B, C, M, X	33 (1080)
12674	7117	2017 Aug 30, N11E58	2017 Sep 12, N16W91	36, 15; B, C	34 (980)
12675	7120	2017 Sep 01, S07W36	2017 Sep 06, S07W91	–	5 (50)
12676	7123	2017 Sep 03, S10W48	2017 Sep 07, S09W91	–	6 (30)
12677	7122	2017 Sep 04, N19E53	2017 Sep 15, N17W91	1; B	4 (20)
12678	7127	2017 Sep 06, N11E33	2017 Sep 15, N11W89	2; C	6 (40)
12679	7117	2017 Sep 08, N14W39	2017 Sep 12, N16W91	1; B	4 (10)
12680	7131	2017 Sep 11, N09E54	2017 Sep 23, N07W91	8, 2; B, C	3 (190)
12681	7144	2017 Sep 21, S12E61	2017 Oct 03, S13W91	11; B	8 (120)
12682	7147	2017 Sep 25, S09E57	2017 Oct 07, S11W91	11; B	7 (230)
12683	7148	2017 Sep 26, N11E62	2017 Oct 08, N13W91	39, 3; B, C	6 (440)
12684	7164	2017 Oct 16, N11W46	2017 Oct 20, N11W91	–	2 (10)
12685	7169	2017 Oct 22, S11E60	2017 Nov 02, S09W89	2, 1; B, M	4 (70)
12686	7171	2017 Oct 24, N12E53	2017 Nov 04, N13W91	2; B	3 (40)
12687	7189	2017 Nov 15, S08E52	2017 Nov 26, S09W91	10; B	5 (90)
12688	7190	2017 Nov 18, N11W44	2017 Nov 22, N11W91	1; B	2 (10)
12689	7192	2017 Nov 26, N13W20	2017 Dec 02, N13W91	6; B	5 (60)
12690	7202	2017 Dec 07, N07W29	2017 Dec 12, N06W91	1; B	3 (10)
12691	7203	2017 Dec 11, S03E30	2017 Dec 20, S03W91	–	3 (10)
12692	7211	2017 Dec 21, N16E33	2017 Dec 31, N17W91	18; B	12 (160)
12693	7222	2018 Jan 05, N18W52	2018 Jan 09, N20W91	1; B	3 (20)
12694	7227	2018 Jan 09, S32W15	2018 Jan 15, S32W91	–	3 (10)
12695	7228	2018 Jan 12, S08W71	2018 Jan 14, S09W91	1; B	2 (10)
12696	7229	2018 Jan 16, S11E13	2018 Jan 25, S12W91	7; B	3 (30)
12697	7235	2018 Jan 31, S10E36	2018 Feb 09, S09W91	3; B	5 (10)
12698	7236	2018 Feb 03, S09W07	2018 Feb 14, S03W91	1; B	1 (10)